AAAS
Energy Material Advances
Volume 2022, Article ID 9765710, 12 pages
https://doi.org/10.34133/2022/9765710

Energy Material Advances
A SCIENCE PARTNER JOURNAL

Research Article

Size-Dependent Reaction Mechanism of λ-MnO_2 Particles as Cathodes in Aqueous Zinc-Ion Batteries

Zhichu Tang,[1] **Wenxiang Chen**,[1,2] **Zhiheng Lyu**,[1,2] **and Qian Chen**[1,2,3,4,5]

[1]*Department of Materials Science and Engineering, University of Illinois at Urbana–Champaign, Urbana, Illinois 61801, USA*
[2]*Materials Research Laboratory, University of Illinois at Urbana–Champaign, Urbana, Illinois 61801, USA*
[3]*Department of Chemistry, University of Illinois at Urbana–Champaign, Urbana, Illinois 61801, USA*
[4]*Department of Chemical and Biomolecular Engineering, University of Illinois at Urbana–Champaign, Urbana, Illinois 61801, USA*
[5]*Beckman Institute of Advanced Science and Technology, University of Illinois at Urbana–Champaign, Urbana, Illinois 61801, USA*

Correspondence should be addressed to Qian Chen; qchen20@illinois.edu

Received 28 September 2021; Accepted 6 January 2022; Published 9 February 2022

Manganese dioxide (MnO_2) with different crystal structures has been widely investigated as the cathode material for Zn-ion batteries, among which spinel λ-MnO_2 is yet rarely reported because Zn-ion intercalation in spinel lattice is speculated to be limited by the narrow three-dimensional tunnels. In this work, we demonstrate that Zn-ion insertion in spinel lattice can be enhanced by reducing particle size and elucidate an intriguing electrochemical reaction mechanism dependent on particle size. Specifically, λ-MnO_2 nanoparticles (NPs, ~80 nm) deliver a high capacity of 250 mAh/g at 20 mA/g due to large surface area and solid-solution type phase transition pathway. Meanwhile, severe water-induced Mn dissolution leads to the poor cycling stability of NPs. In contrast, micron-sized λ-MnO_2 particles (MPs, ~0.9 μm) unexpectedly undergo an activation process with the capacity continuously increasing over the first 50 cycles, which can be attributed to the formation of amorphous MnO_x nanosheets in the open interstitial space of the MP electrode. By adding $MnSO_4$ to the electrolyte, Mn dissolution can be suppressed, leading to significant improvement in the cycling performance of NPs, with a capacity of 115 mAh/g retained at 1 A/g for over 500 cycles. This work pinpoints the distinctive impacts of the particle size on the reaction mechanism and cathode performance in aqueous Zn-ion batteries.

1. Introduction

Although Li-ion batteries (LIBs) dominate the commercial market in recent years, limited supplies of Li, high cost, potential safety issues, and environmental concerns may inhibit their future development [1–3]. To satisfy the increasing demand for large-scale energy storage, aqueous Zn-ion batteries (ZIBs) have attracted considerable attention because of abundant Zn resources, low cost, high volumetric energy density, and good safety [4–6]. Among the known cathode materials for ZIBs, Mn-based oxides are mostly investigated owing to their remarkable diversity in crystal structures, high theoretical energy density, low cost, and environmental friendliness [5, 6]. The performance of MnO_2 with different crystalline polymorphs has been reported, including tunnel type α-MnO_2 [4, 7], β-MnO_2 [8], γ-MnO_2 [9], layered type δ-MnO_2 [10, 11], and spinel type λ-MnO_2 [12]. α-MnO_2 (2×2 tunnels, 4.6 Å × 4.6 Å) and δ-MnO_2 (interlayer space, ~7 Å) show the best electrochemical properties because the large lattice spacings favor Zn-ion diffusion, while λ-MnO_2 with limited three-dimensional (3D) tunnels is speculated to be unfavorable for Zn-ion insertion due to strong electrostatic barrier [13–15]. Interestingly, Yuan et al. recently reported that λ-MnO_2 nanoparticles (NPs) can exhibit a high capacity at low current rate [12]. Nonetheless, the factors and associated mechanism contributing to the high capacity are still yet to be investigated. One possible explanation is that the use of NPs may facilitate Zn-ion insertion and improve the capacity.

λ-MnO_2 has cubic spinel structure, with Mn and O ions occupying the octahedral 16d and 32e sites, respectively. Ideally, metal ions such as Zn^{2+} can insert into or extract from the tetragonal sites with the spinel structure maintained

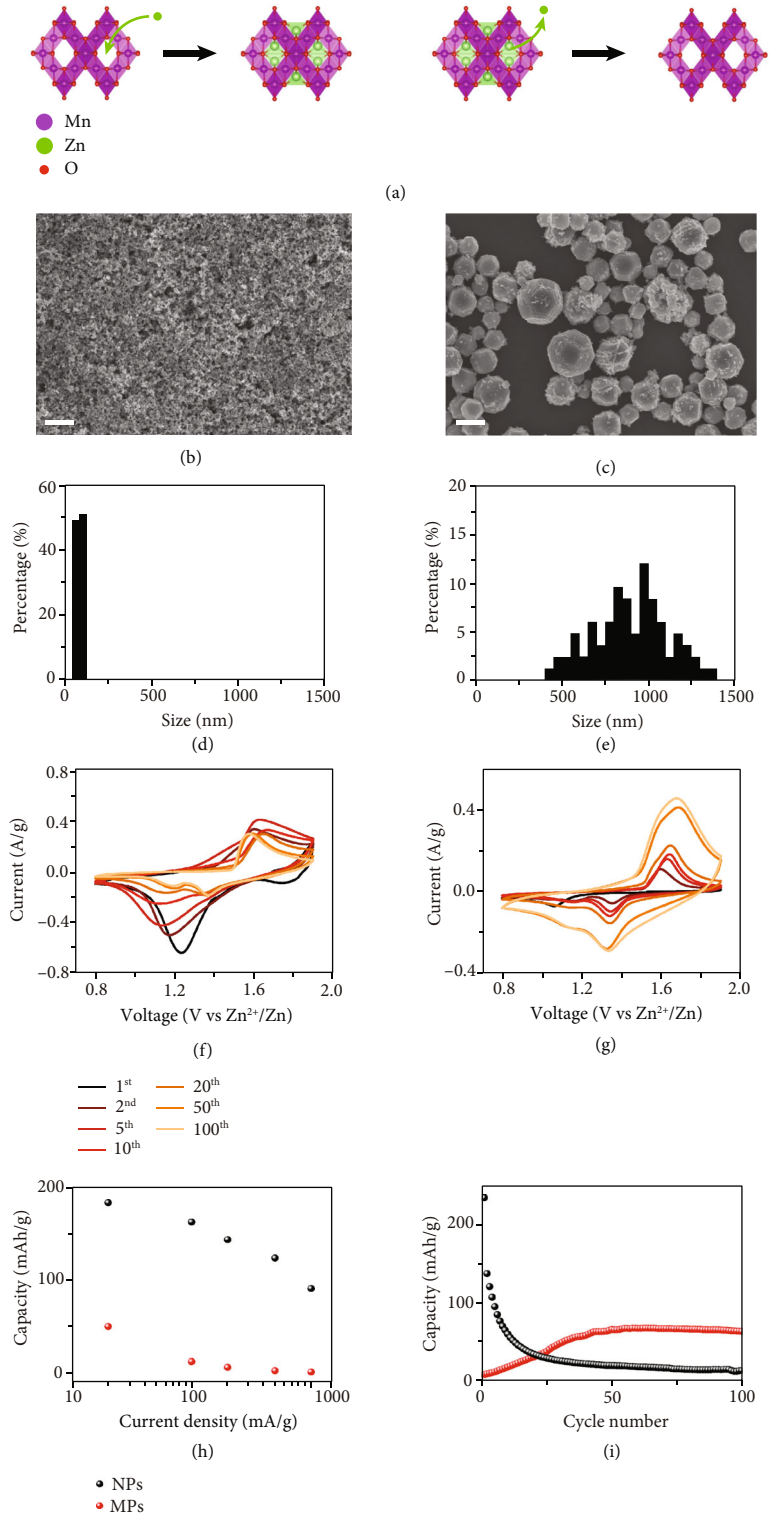

FIGURE 1: (a) Schematic of insertion/extraction of Zn^{2+} in λ-MnO_2 lattice. SEM images of (b) NPs and (c) MPs. Scale bars: 1 μm. Particle size distribution of (d) NPs and (e) MPs. CV curves of (f) NPs and (g) MPs at 0.5 mV/s for different cycles. (h) Rate performance of NPs and MPs within 0.8–1.9 V. Each capacity is the average value of five successive cycles. (i) Cycling performance of NPs and MPs at 200 mA/g.

(Figure 1(a)). In our previous work, the effect of particle size on Mg-ion intercalation in λ-MnO_2 has been thoroughly studied, where we show that reducing particle size can enhance Mg-ion intercalation [16]. This effect can be attributed to the solid-solution type phase transition pathway of λ-MnO_2 NPs from cubic to tetragonal phase during Mg-ion insertion, which minimizes lattice mismatch and energy penalty for phase transformation.

Herein, we further illustrate the relations among the particle size, Zn-ion intercalation, side reactions, and the resulting electrochemical performance in ZIBs, by investigating λ-MnO_2 NPs (~80 nm) and micron-sized particles (MPs) (~900 nm) as a model system. Through X-ray diffraction (XRD), scanning electron microscopy (SEM), transmission electron microscopy (TEM), and energy-dispersive X-ray spectroscopy (EDX), we show that reducing particle size enhances Zn-ion insertion in spinel lattice, but at the same time, severe water-induced Mn dissolution leads to quick capacity degrading. In contrast, MPs undergo an activation process due to the formation of amorphous MnO_x nanosheets in the open spacings of the electrode during cycling, which can reduce charge transfer resistance and contribute to the capacity. This paper highlights the complicated and nonmonotonic size effects of cathode materials on the reaction mechanism and electrochemical property of ZIBs, which offers guidelines for integrating nanoengineering and high-performance cathode materials design for aqueous ZIBs.

2. Experimental

2.1. Materials. Lithium manganese oxide ($LiMn_2O_4$) (>99%, Sigma-Aldrich), hydrochloric acid (99.999%, 36.5% min, Alfa Aesar), zinc sulfate monohydrate (99.9%, Sigma-Aldrich), manganese sulfate monohydrate (99%, Alfa Aesar), 1-methyl-2-pyrrolidinone (NMP) (99.5%, Sigma-Aldrich), carbon black (Super P Conductive, 99+%, Alfa Aesar), polyvinylidene fluoride (PVDF) (>99.5%, MTI Corporation), 304 stainless steel shim (6304-1, Trinity Brand Industry), filter paper (1001-090, Whatman), and zinc foil (0.25 mm thick, 99.98%, Alfa Aesar) are all directly used as purchased. All water used in this work is nanopure deionized (DI) water (18.2 MΩ·cm at 25°C) processed by a Milli-Q Advantage A10 system.

2.2. Preparation of λ-MnO_2 Particles. The λ-MnO_2 particles are prepared by acid leaching from as-purchased $LiMn_2O_4$ particles. Specifically, 2 g of $LiMn_2O_4$ particles is soaked in 200 mL of aqueous HCl solution (0.1 M) and stirred at 300 rpm for 13.5 h to extract Li^+ ions. The dispersion is then filtered and thoroughly rinsed with DI water to get the partially delithiated $Li_xMn_2O_4$ particles (λ-MnO_2) on the filter paper, which are dried at room temperature and collected for later use.

In order to study the effect of particle size on the performance of λ-MnO_2, λ-MnO_2 NPs and MPs are collected by several steps of centrifugation (Eppendorf 5804 centrifuge). First, 0.2 g of λ-MnO_2 particles is dispersed in 30 mL of DI water in a centrifuge tube by sonication.

To collect NPs, the dispersion is centrifuged at 3000 rpm for 5 min. The supernatant is then collected for one more round of centrifugation at 8000 rpm for 5 min. Next, the sediment at the bottom of the tube is collected and redispersed in DI water by sonication and finally dried at room temperature to get NPs.

To collect MPs, the dispersion is centrifuged at 2000 rpm for 2 min. Then, the supernatant is removed, and the sediment is collected and redispersed in 30 mL DI water for two more rounds of centrifugation (2000 rpm, 2 min), each time with the supernatant removed and the sediment redispersed in 30 mL of DI water. Finally, the suspension is dried at room temperature to get MPs.

2.3. Preparation of Working Electrodes. Working electrodes are prepared by mixing NPs (or MPs) with carbon black and PVDF at a fixed weight ratio of 8 : 1 : 1 in a desirable amount of NMP solvent in an agate mortar. The mixture is ground for 15 min in the glovebox to achieve uniform slurry. The slurry is then cast on the stainless steel shim with a film casting doctor blade (MTI) to control the thickness of the slurry film (~15 μm). The corresponding mass loading is ~2 mg/cm^2. The stainless steel shim cast with slurry film is then left in the vacuum oven to dry overnight at room temperature to obtain the working electrode. Finally, the working electrode is punched into circular pieces (12 mm in diameter) for electrochemical tests.

2.4. Electrochemical Measurements. A custom-made Swagelok cell and a multichannel potentiostat (VMP3, Bio-Logic Science Instruments) are used for all the electrochemical measurements. The cell is assembled using MnO_2 electrode as the cathode, glass fiber as the separator, Zn foil as the anode, and 0.2 M $ZnSO_4$ aqueous solution as the electrolyte. The galvanostatic measurements are conducted within the voltage range of 0.8 V to 1.9 V (vs. Zn^{2+}/Zn) under different current densities. Cyclic voltammetry (CV) curves are measured in the voltage range of 0.8 V to 1.9 V at various scan rates. The electrochemical impedance spectroscopy (EIS) is performed with an amplitude of 10 mV in the frequency range from 200 kHz down to 5 mHz.

2.5. Characterization. X-ray diffraction (XRD, Bruker D8 Advance) with Cu K_α radiation (λ = 1.5418 Å) is used to characterize the MnO_2 electrodes before and after electrochemical measurements. Scanning electron microscopy (SEM, Hitachi 4800) is used to monitor the size of λ-MnO_2 particles after centrifugation and the surface morphology of MnO_2 electrodes before and after electrochemical measurements. Transmission electron microscopy (TEM) and selected-area electron diffraction (SAED) are performed on JEOL 2100 Cryo TEM with a LaB_6 emitter at 200 kV. Energy-dispersive X-ray spectroscopy (EDX) and high-angle annular dark-field (HAADF) imaging are performed on Themis Z analytical scanning TEM (STEM, Thermo Fisher) as operated at 300 kV. X-ray photoelectron spectroscopy (XPS, Kratos Axis ULTRA) is used for the surface composition analysis of the electrodes after cycling.

3. Results and Discussion

The λ-MnO_2 particles are prepared from as-purchased $LiMn_2O_4$ particles by simple acid leaching (0.1 M HCl) to extract Li^+ ions. The XRD patterns of $LiMn_2O_4$ and λ-MnO_2 (Figure S1) show that the crystal structure of $LiMn_2O_4$ (cubic phase, $Fd\bar{3}m$ group) is maintained after acid leaching, with the diffraction peaks shifting towards higher angles, indicating the decrease of lattice parameter from 8.219 Å to 8.042 Å. The composition of λ-MnO_2 is

estimated to be $Li_{0.12}Mn_2O_4$ according to the lattice parameter [17]. The morphology of the particles has no obvious change after delithiation, with particle size highly polydispersed, ranging from several micrometers to tens of nanometers (Figure S2). To study the effect of particle size on the performance of λ-MnO_2, we employ several steps of centrifugation (see Section 2.2) to obtain λ-MnO_2 NPs (80 ± 15 nm, Figures 1(b) and 1(d)) and MPs (900 ± 295 nm, Figures 1(c) and 1(e)). The HAADF image and corresponding SAED pattern present the single-crystal nature of NPs (Figure S3).

A custom-made Swagelok cell is used for all the electrochemical measurements, with λ-MnO_2 electrode as the cathode, glass fiber as the separator, Zn foil as the anode, and 0.2 M $ZnSO_4$ aqueous solution as the electrolyte. CV curves of NPs (Figure 1(f)) and MPs (Figure 1(g)) are measured between 0.8 and 1.9 V (vs. Zn^{2+}/Zn) at a scan rate of 0.5 mV/s to reveal the redox reactions in the battery. For NPs, there is one strong peak at around 1.2 V and one relatively weak peak at around 1.4 V within the first discharge. According to the previous studies [18, 19], the peak at 1.2 V corresponds to the intercalation of Zn^{2+}, the current intensity of which drops during cycling, with the peak position shifting towards lower potentials, indicating the increase of Zn-ion insertion resistance. In comparison, MPs have one reduction peak at around 1.1 V in the first cycle, while two reduction peaks can be observed at 1.15 V and 1.35 V in the following cycles. The current intensity of the reduction peaks for MPs is much smaller than that of NPs at the beginning, which means lower electrochemical activity. However, the gradual increase of current during cycling suggests an activation process for MPs. The rate and cycling performance of NPs and MPs are consistent with the CV results. Figure 1(h) shows the discharge capacities of NPs and MPs at different current rates. Each capacity is the average value of five successive cycles. The capacities of NPs at 20, 100, 200, 500, and 1000 mA/g are 184, 163, 144, 124, and 91 mAh/g, respectively. In comparison, MPs exhibit much lower discharge capacities at these current rates. However, although NPs can deliver higher initial capacity, the cycling stability is poor, with only 10% capacity retained after 50 cycles at 200 mA/g, while MPs undergo an activation process in the first 50 cycles and then become stable with the capacity maintained at around 65 mAh/g (Figure 1(i)).

To investigate why NPs show better rate performance and higher initial capacity than MPs but suffer quick capacity fading, NP/Zn batteries are first charged to 1.9 V to remove residual Li^+ and then discharged to 1.4 V, 1.3 V, and 0.8 V, respectively, at a current density of 20 mA/g (Figure 2(a)). It is notable that the discharge capacity is larger than charge capacity in the first cycle (Figure 2(a)), but this difference does not persist in the later cycles (Figure S4). We attribute this irreversible capacity in the first battery cycle to the formation of solid electrolyte interphase (SEI) film on the electrode surface or the trapping of Zn ions inside the spinel lattice due to lattice distortion during Zn-ion insertion, which has been observed in Li-ion batteries [20–23]. Electrodes are then collected at these cutoff voltages for XRD characterization (Figure 2(b)). When the battery is discharged to 0.8 V, the peaks of cubic spinel λ-MnO_2 disappear, while a few new peaks emerge at 18.2°, 33.0°, and 36.4°, which can correspond to tetragonal spinel $ZnMn_2O_4$. To closely monitor the phase transition process, a zoomed-in view of the XRD pattern in the vicinity of c (111) peak is also provided (Figure 2(c)). The c (111) peak gradually shifts towards lower angles during Zn-ion insertion and finally turns into t (101), indicating a solid-solution type phase transition from cubic spinel λ-MnO_2 to tetragonal spinel $ZnMn_2O_4$. EDX mapping of NPs collected from state "C" also proves successful Zn-ion intercalation (Figure 2(f)). The uniform distribution of Zn^{2+} in the particle further confirms the solid-solution type phase transformation. When the battery is recharged to 1.9 V, the t (101) peak shifts to higher angles but does not return to the original position of c (111) (Figure 2(c)). This means only part of the inserted Zn ions can be extracted from the spinel lattice, resulting in the irreversible capacity loss for the first cycle. Aside from Zn-ion insertion, proton insertion is also widely discussed for different phases of MnO_2, often resulting in the formation of MnOOH that is detectable by XRD [4, 18, 24]. However, as shown in Figures 2(b) and 3(b), in our system, no obvious MnOOH peaks are detected by XRD for the cathode particles collected at different cutoff voltages, indicating that proton insertion is not the main reaction mechanism for spinel λ-MnO_2. It is also notable that the peaks labeled with red "*" match well with $Zn_4SO_4(OH)_6{\bullet}4H_2O$ (ZHS). The SEM image of the electrode collected from state "C" (Figure 2(d)) shows the formation of ZHS flakes on the electrode surface, consistent with the observations in previous studies [25–27]. Part of these flakes disappears after recharging to state "D" (Figure 2(e)). It has been reported that the formation of ZHS is due to the increase of pH in the electrolyte during discharge, which is caused by the water-induced Mn dissolution ($MnO_2 + 2H_2O + 2e^- \longrightarrow Mn^{2+} + 4OH^-$) [25]. Therefore, the large amounts of ZHS detected after discharge represent severe Mn dissolution, which causes the loss of active cathode materials and leads to capacity fading.

As a comparison, MP/Zn batteries are also charged and discharged at 20 mA/g (Figure 3(a)) and then characterized in the same way as NPs. The initial discharge capacity of MPs is 50 mAh/g, which is much smaller than that of NPs (250 mAh/g). This observation can be explained by the XRD patterns of MPs at different cutoff voltages, which show negligible changes for the diffraction peaks of λ-MnO_2 during discharge (Figures 3(b) and 3(c)), indicating limited Zn-ion insertion within the first cycle. ZHS peaks are also detected, with the peak intensity relatively weaker than that of NPs. The SEM image of the electrode collected from state "C" is consistent with the XRD results, showing smaller ZHS flakes on the electrode surface (Figure 3(d)), which totally disappear (Figure 3(e)) after recharging to state "D." Less ZHS formation indicates weaker Mn dissolution reaction compared to NPs due to smaller surface area (51.6 m^2/g for NPs and 15.1 m^2/g for MPs [16]). Element mapping of MPs collected from state "C" shows that Zn ions accumulate on the surface of MPs, forming a core-shell

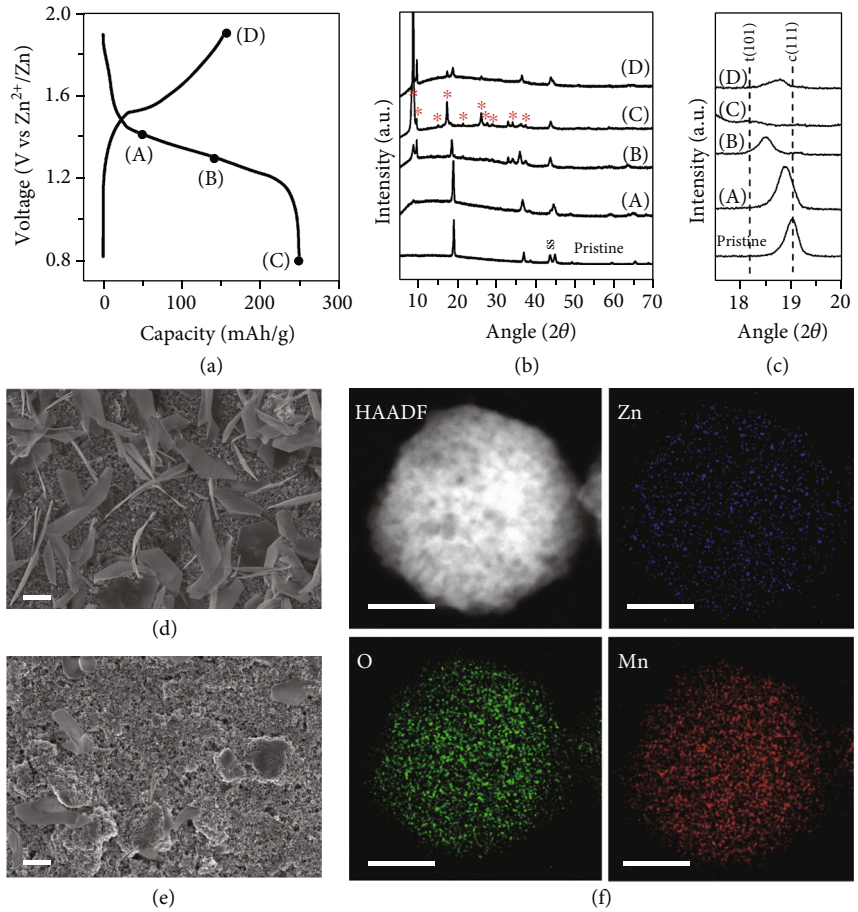

FIGURE 2: (a) Galvanostatic charge and discharge curves at 20 mA/g for NPs with different cutoff voltages (A–D) noted at which electrodes are collected for XRD characterization. (b) XRD patterns of pristine NP electrode and electrodes collected at various cutoff voltages during discharge (A–C) and recharge (D) noted in (a). (c) Zoomed-in view of the features in the vicinity of c (111) peak. Diffraction peaks of cubic spinel λ-MnO_2 (PDF#: 44-0992), tetragonal spinel $ZnMn_2O_4$ (PDF#: 24-1133), stainless steel shim (PDF#: 06-0696), and zinc hydroxide sulfates ($Zn_4SO_4(OH)_6 \bullet 4H_2O$ PDF# 44-0673; $Zn_4SO_4(OH)_6 \bullet 3H_2O$ PDF#: 39-0689) are labeled as c, t, ss, and *, respectively. SEM images of electrodes (d) collected from "C," and (e) collected from "D." Scale bars of (d) and (e): 10 μm. (f) HAADF image of a single NP collected from "C" and its corresponding elemental mapping (Zn, Mn, and O) by EDX. Scale bars of (f): 20 nm.

structure, due to the slow Zn-ion diffusivity (Figure 3(f)). Based on these results, the enhanced initial capacity and rate performance of NPs can be attributed to the solid-solution type phase transition pathway, where the minimized lattice mismatch and energy penalty for accommodating new phases facilitate Zn-ion intercalation [16].

Next, CV curves of NPs (Figure 4(a)) and MPs (Figure 4(b)) at varying scan rates are measured to study the mechanism of charge storage for λ-MnO_2 with different particle sizes. The area under the curve represents the total stored charge contributed by the diffusion-limited faradaic process (intercalation) and the non-diffusion-limited redox pseudocapacitance. The relation between current i and scan rate v at a fixed voltage V can be expressed by a combination of these two factors:

$$i(V) = a_1 v + a_2 v^{0.5}, \quad (1)$$

where $a_1 v$ and $a_2 v^{0.5}$ represent capacitance and intercalation, respectively [16, 28]. The values of a_1 and a_2 can be obtained by linearly fitting $i(V)/v^{0.5}$ as a function of $v^{0.5}$ at different voltages based on the CV curves. Then, CV curves representing intercalation (red) and capacitance (blue) are replotted at 2 mV/s as an example according to a_1 and a_2 (Figure S5a,b). The stored charge corresponding to each contribution can be calculated from the area under each curve. As Figure 4(c) shows, for fresh electrodes, the total stored charge for NPs is 105 mAh/g, with 16% contributed by capacitance and 84% contributed by intercalation. In comparison, MPs only exhibit a total charge storage of 22 mAh/g, with 10% and 90% corresponding to capacitance and intercalation, respectively. The higher capacitance contribution of NPs can be attributed to the larger surface area than that of MPs, while the greatly improved intercalation is due to the solid-solution type phase transition pathway [16, 29]. Similarly, CV curves of NPs (Figure 4(d)) and MPs (Figure 4(e)) at varying scan rates are also measured after 50 cycles of galvanostatic discharge and charge at 200 mA/g. As shown in Figure 4(f),

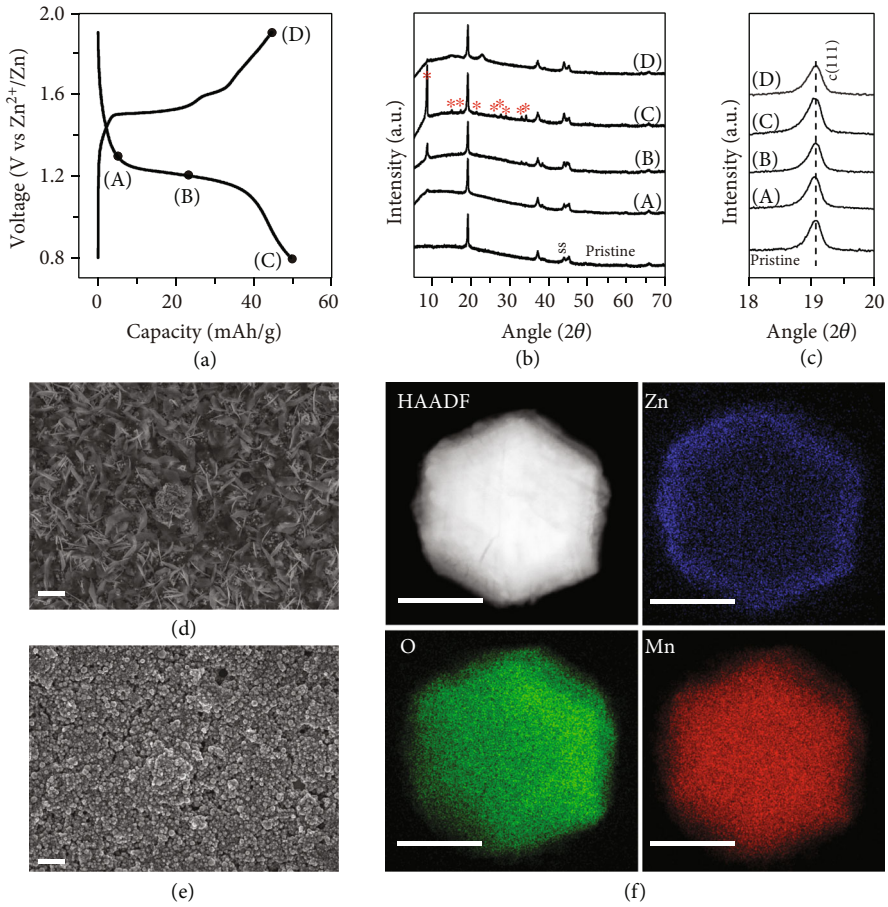

Figure 3: (a) Galvanostatic charge and discharge curves at 20 mA/g for MPs with different cutoff voltages noted at which electrodes are collected for XRD characterization. (b) XRD patterns of pristine MP electrode and electrodes collected at various cutoff voltages during discharge (A–C) and recharge (D) as noted in (a). (c) Zoomed-in view of the features in the vicinity of c (111) peak. Diffraction peaks of cubic spinel λ-MnO_2 (PDF#: 44-0992), stainless steel shim (PDF#: 06-0696), and zinc hydroxide sulfates ($Zn_4SO_4(OH)_6{\bullet}4H_2O$ PDF#: 44-0673; $Zn_4SO_4(OH)_6{\bullet}3H_2O$ PDF#: 39-0689) are labeled as c, ss, and *, respectively. SEM images of electrodes (d) collected from "C" and (e) collected from "D." Scale bars of (d) and (e): 10 μm. (f) HAADF image of a single MP collected from "C" and its corresponding elemental mapping (Zn, Mn, and O) by EDX. Scale bars of (f): 500 nm.

the total stored charge for NPs is decreased to 35 mAh/g after cycling (17% by capacitance and 87% by intercalation). In contrast, the stored charge for MPs is increased to 50 mAh/g (8% by capacitance and 92% by intercalation), which means the activation process of MPs can facilitate Zn-ion intercalation. The enhanced Zn-ion insertion can be proved by the XRD patterns of MPs after different cycles of discharge (Figure 4(g)). From the detailed view of the features in the vicinity of c (111) peak (Figure 4(h)), a new t (101) peak can be observed after 50 cycles, demonstrating the formation of tetragonal $ZnMn_2O_4$ phase due to Zn-ion insertion. The element mapping of MPs after 100^{th} discharge (Figure 4(i)) shows more uniform Zn-ion distribution compared to that of the first discharge, which further supports the improved Zn-ion intercalation after the activation process.

To better understand the degrading mechanism of NPs and the activation process of MPs, EIS measurements are conducted after different cycles of charge (Figures 5(a) and 5(b)). According to the equivalent circuit model (Figure 5(c)), the values of series resistance (R_s), interfacial resistance between the electrolyte and electrode (R_i), and charge transfer resistance (R_{ct}) can be obtained by EIS fitting. As Table S1 shows, the series resistances of NPs (~9 Ω) and MPs (~8 Ω) do not show significant changes during cycling. After 100 cycles, the interfacial resistances of NPs and MPs increase from 5 to 11 Ω and 4 to 13 Ω, respectively, which may indicate a SEI film formation on the particle surface [30]. However, the interfacial resistance is negligible compared to the charge transfer resistance. The charge transfer resistance of NPs increases rapidly from 83 to 285 Ω during the first 50 cycles, which can be attributed to the formation of a passivated layer on the particle surface due to the severe reactions with the electrolyte [31]. The XRD patterns of NPs after different cycles of charge and discharge show negligible shift in peak positions (Figure S6a,b), indicating suppressed Zn-ion insertion/extraction due to the passivated layer. In comparison, the charge transfer resistance of MPs increases from 350 to 710 Ω during the first 20 cycles, which is much larger than

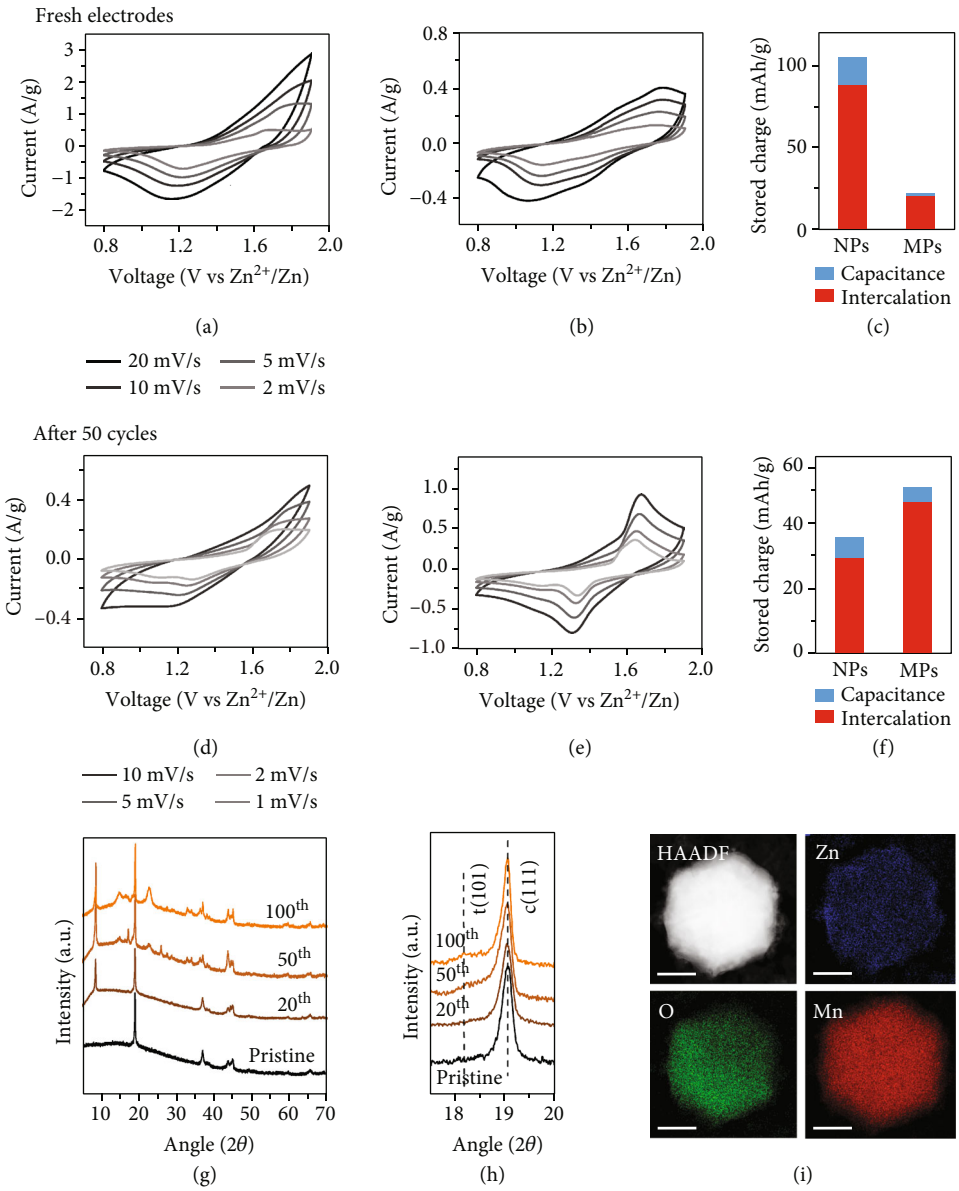

FIGURE 4: CV curves with different scan rates for fresh (a) NPs and (b) MPs. (c) Corresponding column graph of charge storage contributions at 2 mV/s. CV curves of (d) NPs and (e) MPs after operating at 200 mA/g for 50 cycles. (f) Corresponding column graph of charge storage contributions at 2 mV/s. (g) XRD patterns of MPs after different cycles of discharge. (h) Zoomed-in view of the features in the vicinity of c (111) peak. (i) HAADF image of a single MP after 100th discharge and its corresponding elemental mapping (Zn, Mn, and O) by EDX. Scale bars: 500 nm.

that of NPs, resulting in lower electrochemical activity. Interestingly, in the following cycles, R_{ct} drops dramatically to 123 Ω and then becomes stable after 50 cycles. The corresponding XRD patterns show that the t (101) peaks disappear after charge (Figure S6c,d), suggesting good reversibility of Zn-ion insertion/extraction. Therefore, we hypothesize that such significant impedance decrease may indicate a new phase formation, which can enhance Zn-ion diffusion and thus improve the capacity of MPs.

To confirm this hypothesis, the surface morphology change of NPs and MPs after cycling is studied by SEM and TEM. The SEM images show that there is nanosheet formation covering the electrode surface during cycling for both NPs and MPs (Figure 6). The composition of the surface layer can be confirmed by XPS measurements. For both NP electrode and MP electrode, a peak is detected at 642.9 eV, which corresponds to Mn $2p_{3/2}$ (Figure S7). According to previous studies, these nanosheets are MnO_x generated from the oxidation of Mn^{2+} in the electrolyte during charge, which can reduce charge transfer resistance and contribute to the capacity [32]. Therefore, the activation process of MPs can be attributed to the formation of MnO_x nanosheets during cycling. However, this conclusion still cannot explain why the nanosheet formation does not improve the cycling performance of NPs. For further investigation, SEM images of the cross-

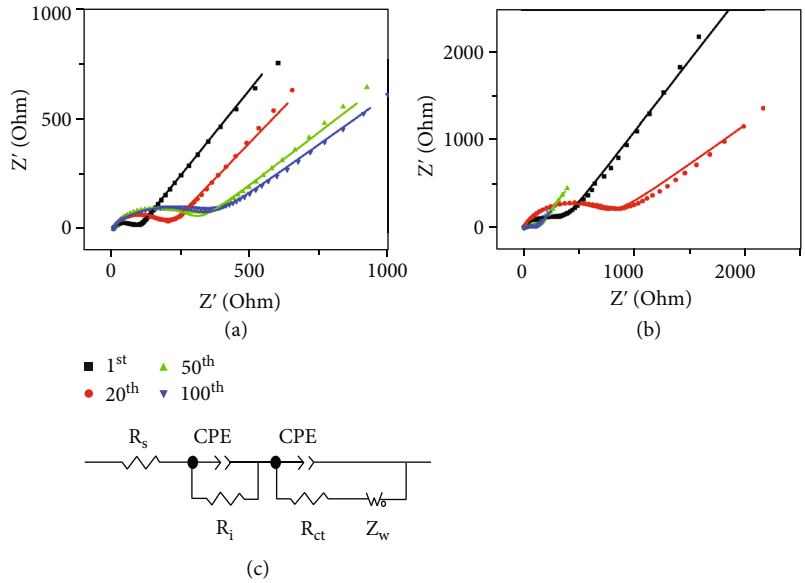

Figure 5: Nyquist diagrams of EIS measurements for (a) NPs and (b) MPs after different cycles of charge. The scatters are experimental data while the solid lines are fitted curves. (c) Equivalent circuit model to fit the EIS data, where R_s, R_i, R_{ct}, CPE, and Z_w represent series resistance, interfacial resistance between the electrolyte and electrode, charge transfer resistance, constant phase element, and Warburg diffusion process, respectively.

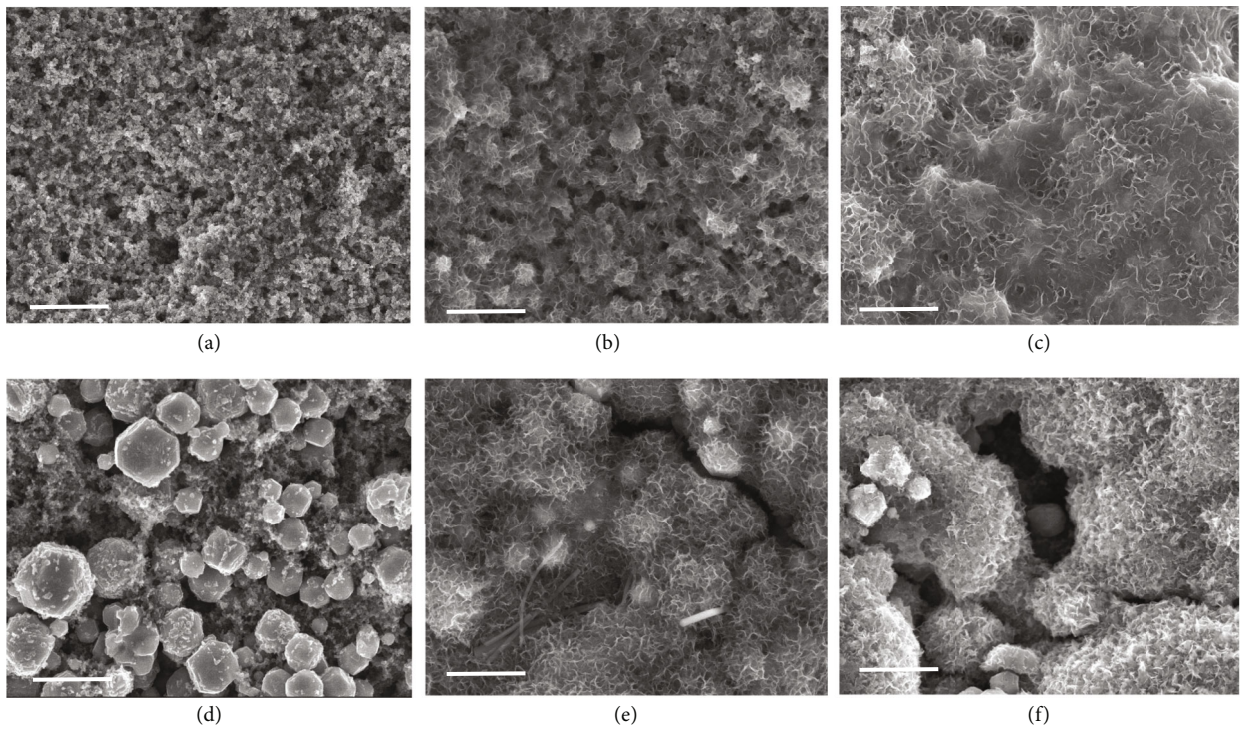

Figure 6: SEM images of NP electrode: (a) fresh, (b) after 20th charge, and (c) after 100th charge at 200 mA/g. SEM images of MP electrode: (d) fresh, (e) after 20th charge, and (f) after 100th charge at 200 mA/g. Scale bars: 2 μm.

section of the electrodes are taken, from which we can see the nanosheets only form on the top layer of the NP electrode, while they can fill throughout the open spacings of the MP electrode (Figure S8). One possible reason for this observation is that the large spacings between MPs provide enough room for the nanosheet formation while the more densely packed NPs cannot. As a result, the nanosheets can improve the interconnection between MPs and deliver more contribution to the capacity of MPs than NPs. This understanding suggests the importance of

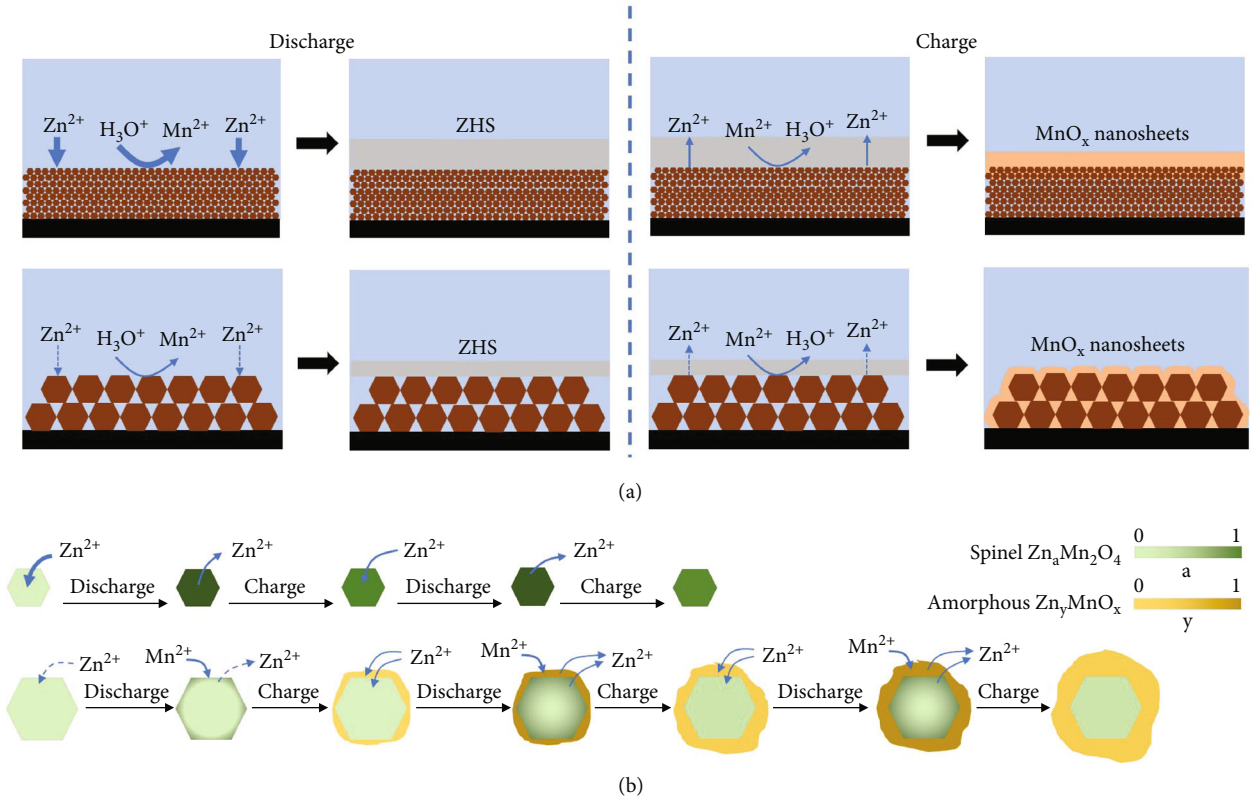

FIGURE 7: Schematic of the reactions and morphology change for (a) NP electrode and MP electrode and (b) single NP and MP during discharge and charge.

engineering the porosity of microstructures in the electrode design. The TEM image of MPs after 100 cycles (Figure S9c) also shows the formation of nanosheets covering the MP surface. The corresponding SAED pattern (Figure S9d) exhibits the amorphous character of the nanosheets. In contrast, there is no obvious surface morphology change for most of NPs after cycling (Figure S9a,b), which is consistent with the cross-sectional SEM results. The HAADF images of NPs and MPs before and after 100 cycles show that the structure of the particles is maintained during cycling (Figure S10a,b), without severe corrosion or structural collapse. This observation can further prove that the continuous increase of capacity for MPs is due to the formation of amorphous MnO_x nanosheets instead of possible increase in particle surface area due to particle collapsing.

According to the discussions above, the main reactions on the λ-MnO_2 electrode in ZIBs can be concluded by the following equations:

$$Zn^{2+} + 2MnO_2 + 2e^- \rightleftharpoons ZnMn_2O_4 \quad (2)$$

$$MnO_2 + 2H_2O + 2e^- \rightleftharpoons Mn^{2+} + 4OH^- \quad (3)$$

$$4Zn^{2+} + 6OH^- + SO_4^{2-} + 4H_2O \rightleftharpoons Zn_4SO_4(OH)_6 \bullet 4H_2O \quad (4)$$

As the schematic shows (Figure 7(a)), water-induced Mn dissolution (Equation (3)) occurs on both NP and MP electrodes during discharge. However, this reaction is more drastic for NPs due to their large surface area, which causes the degrading of capacity. As a result, more ZHS flakes form (Equation (4)) on the NP electrode surface compared to MPs. During charge, the dissolved Mn^{2+} in the electrolyte will be oxidized and deposited back to the electrode to form amorphous MnO_x nanosheets. The MnO_x nanosheets can only overlay the top of the electrode for NPs, while they can fill the open spacings between MPs. At the same time, the H^+ generated from the oxidation of Mn^{2+} will cause the dissolution of ZHS flakes on the electrode surface. At the single-particle level (Figure 7(b)), Zn-ion insertion (Equation (2)) in NPs is enhanced due to large surface area and solid-solution type phase transition pathway, resulting in a homogeneous tetragonal $ZnMn_2O_4$ phase formation. However, the inserted Zn ions are only partially extractable due to the strong energy barrier for Zn-ion extraction. In contrast, Zn-ion insertion is limited for fresh MPs, with Zn^{2+} accumulating on the particle surface, forming a core-shell structure. During charge, amorphous MnO_x nanosheets will form on the surface of MPs, which can reduce charge transfer resistance and also act as a host for Zn-ion insertion. The gradual growth of MnO_x nanosheets during cycling can correspond to the activation process of MPs.

After figuring out Mn dissolution as the major degrading mechanism of λ-MnO_2 NPs in aqueous ZIB system, a common strategy is applied to improve the cycling stability by adding 0.1 M $MnSO_4$ to the electrolyte, which can effectively reduce Mn dissolution [4]. As a result, the

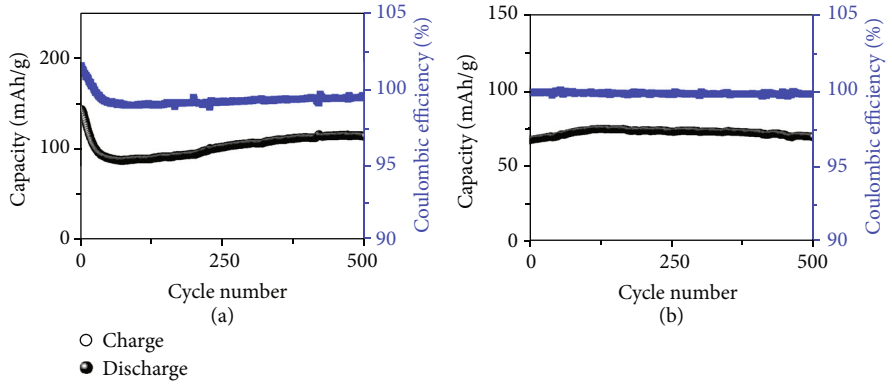

FIGURE 8: Cycling performance of ZIBs using 0.2 M $ZnSO_4$ + 0.1 M $MnSO_4$ as the electrolyte for (a) NPs and (b) MPs after activation at 1 A/g.

cyclingperformance of NPs is significantly improved, with a capacity of 115 mAh/g retained for over 500 cycles at a current rate of 1 A/g (Figure 8(a)). As a comparison, MPs are first activated at 200 mAh/g for 50 cycles, after which the current is increased to 1 A/g for measurement. After activation, the capacity of MPs is maintained at about 70 mAh/g (Figure 8(b)), which is lower than that of NPs. It is also notable that the coulombic efficiencies for both NPs and MPs are around 100%, indicating good reversibility of the battery. The electrochemical performance of λ-MnO_2 NPs with Mn additive in the electrolyte is superior to most of the cathode materials that have been reported (Table S2) [4, 8, 9, 11, 15, 33, 34], demonstrating that λ-MnO_2 can also be a potential cathode material for ZIBs by controlling the particle size and Mn dissolution.

4. Conclusions

In this work, we reveal the effects of particle size on the performance and reaction mechanisms of λ-MnO_2 in aqueous Zn-ion batteries. We show that λ-MnO_2 MPs have limited Zn-ion intercalation initially but undergo an activation process during cycling due to the formation of amorphous MnO_x nanosheets in the open spacings of the electrode. By reducing particle size, a higher capacity of 250 mAh/g can be obtained at 20 mA/g for λ-MnO_2 NPs, which is on account of the enhanced Zn-ion insertion due to large surface area and solid-solution type phase transition pathway. Meanwhile, reducing particle size can also lead to severer water-induced Mn dissolution, which causes the quick capacity degrading of NPs. To improve the cycling stability of NPs, $MnSO_4$ is added to the electrolyte to suppress Mn dissolution. As a result, a capacity of 115 mAh/g can be maintained over 500 cycles at 1 A/g for NPs, exceeding the performance of most Mn oxide-based electrodes. This paper not only highlights the advantages of using NPs as the cathode material for ZIBs but also points out the issues of possibly enhanced side reactions and corresponding solutions, which can offer guidelines for the design of high-performance cathode materials for ZIBs.

Data Availability

All data presented in the paper and the supporting information are available from the corresponding author upon reasonable request.

Conflicts of Interest

The authors declare no conflict of interest.

Authors' Contributions

Z. T., W. X., and Q. C. conceived the experimental design. Z. T. conducted the experiments and analyzed the data. Z. L. contributed to the HAADF images and EDX mapping. The manuscript was prepared by Z. T. under W. X. and Q. C.'s help. All authors have given approval to the final version of the manuscript.

Acknowledgments

We thank Dr. Hyosung An for the help with the EIS measurements. This work was supported by the Energy & Biosciences Institute through the EBI-Shell program and the National Science Foundation under Grant No. 1752517. Experiments were carried out in part in the Materials Research Laboratory Central Research Facilities, University of Illinois.

Supplementary Materials

XRD patterns of LiMn2O4 and λ-MnO2; SEM images of LiMn2O4 and λ-MnO2; TEM image and corresponding SAED pattern of a single NP; CV fitting for NPs and MPs at initial state and after 50th charge at 200 mA/g; XRD patterns of NPs and MPs after different cycles of discharge and charge at 200 mA/g; Mn $2p_{3/2}$ XPS spectra of the electrode surface after 100^{th} charge at 200 mA/g; SEM images of the cross-section of fresh electrodes and electrodes after 100^{th} charge; TEM images of NPs and MPs after 100^{th} charge; HAADF images of MPs before and after 100 cycles; specific values of series resistance, interface resistance, and

charge transfer resistance obtained by EIS fitting for NPs and MPs after different cycles of charge; summary of electrochemical performance of different cathode materials for ZIBs. *(Supplementary Materials)*

References

[1] J. M. Tarascon and M. Armand, "Issues and challenges facing rechargeable lithium batteries," *Nature*, vol. 414, pp. 359–367, 2001.

[2] J. B. Goodenough and K. S. Park, "The Li-ion rechargeable battery: a perspective," *Journal of the American Chemical Society*, vol. 135, no. 4, pp. 1167–1176, 2013.

[3] N. Nitta, F. Wu, J. T. Lee, and G. Yushin, "Li-ion battery materials: present and future," *Materials Today*, vol. 18, no. 5, pp. 252–264, 2015.

[4] H. Pan, Y. Shao, P. Yan et al., "Reversible aqueous zinc/manganese oxide energy storage from conversion reactions," *Nature Energy*, vol. 1, no. 5, article 16039, 2016.

[5] J. Ming, J. Guo, C. Xia, W. Wang, and H. N. Alshareef, "Zinc-ion batteries: materials, mechanisms, and applications," *Materials Science and Engineering: R: Reports*, vol. 135, pp. 58–84, 2019.

[6] C. Li, X. Zhang, W. He, G. Xu, and R. Sun, "Cathode materials for rechargeable zinc-ion batteries: from synthesis to mechanism and applications," *Journal of Power Sources*, vol. 449, p. 227596, 2020.

[7] B. Lee, C. S. Yoon, H. R. Lee, K. Y. Chung, B. W. Cho, and S. H. Oh, "Electrochemically-induced reversible transition from the tunneled to layered polymorphs of manganese dioxide," *Scientific Reports*, vol. 4, p. 6066, 2015.

[8] S. Islam, M. H. Alfaruqi, V. Mathew et al., "Facile synthesis and the exploration of the zinc storage mechanism of β-MnO2nanorods with exposed (101) planes as a novel cathode material for high performance eco-friendly zinc-ion batteries," *Journal of Materials Chemistry A*, vol. 5, no. 44, pp. 23299–23309, 2017.

[9] M. H. Alfaruqi, V. Mathew, J. Gim et al., "Electrochemically induced structural transformation in a γ-MnO2Cathode of a high capacity zinc-ion battery system," *Chemistry of Materials*, vol. 27, no. 10, pp. 3609–3620, 2015.

[10] M. H. Alfaruqi, J. Gim, S. Kim et al., "A layered δ-MnO_2 nanoflake cathode with high zinc-storage capacities for eco-friendly battery applications," *Electrochemistry Communications*, vol. 60, pp. 121–125, 2015.

[11] D. Wang, L. Wang, G. Liang et al., "A superior δ-MnO2-Cathode and a self-healing Zn-δ-MnO2Battery," *ACS Nano*, vol. 13, no. 9, pp. 10643–10652, 2019.

[12] C. Yuan, Y. Zhang, Y. Pan, X. Liu, G. Wang, and D. Cao, "Investigation of the intercalation of polyvalent cations (Mg^{2+}, Zn^{2+}) into λ-MnO_2 for rechargeable aqueous battery," *Electrochimica Acta*, vol. 116, pp. 404–412, 2014.

[13] M. E. Pam, D. Yan, J. Yu et al., "Microstructural engineering of cathode materials for advanced zinc-ion aqueous batteries," *Advanced Science*, vol. 8, no. 1, p. 2002722, 2021.

[14] Z. Rong, R. Malik, P. Canepa et al., "Materials design rules for multivalent ion mobility in intercalation structures," *Chemistry of Materials*, vol. 27, no. 17, pp. 6016–6021, 2015.

[15] N. Zhang, F. Cheng, Y. Liu et al., "Cation-deficient spinel ZnMn2O4Cathode in Zn(CF3SO3)2Electrolyte for rechargeable aqueous Zn-ion battery," *Journal of the American Chemical Society*, vol. 138, no. 39, pp. 12894–12901, 2016.

[16] W. Chen, X. Zhan, B. Luo et al., "Effects of particle size on Mg2+Ion intercalation into λ-MnO2Cathode materials," *Nano Letters*, vol. 19, no. 7, pp. 4712–4720, 2019.

[17] K. Kanamura, H. Naito, T. Yao, and Z. I. Takehara, "Structural change of the $LiMn_2O_4$ spinel structure induced by extraction of lithium," *Journal of Materials Chemistry*, vol. 6, no. 1, pp. 33–36, 1996.

[18] W. Sun, F. Wang, S. Hou et al., "Zn/MnO_2 Battery chemistry with $^{H+}$ and Zn^{2+} Coinsertion," *Journal of the American Chemical Society*, vol. 139, no. 29, pp. 9775–9778, 2017.

[19] H. Zhang, J. Wang, Q. Liu et al., "Extracting oxygen anions from $ZnMn_2O_4$: robust cathode for flexible all-solid-state Zn-ion batteries," *Energy Storage Materials*, vol. 21, pp. 154–161, 2019.

[20] A. L. M. Reddy, M. M. Shaijumon, S. R. Gowda, and P. M. Ajayan, "Coaxial MnO_2/carbon nanotube array electrodes for High-Performance lithium batteries," *Nano Letters*, vol. 9, no. 3, pp. 1002–1006, 2009.

[21] S. Kim, J. Choi, S. M. Bak et al., "Reversible conversion reactions and small first cycle irreversible capacity loss in metal sulfide-based electrodes enabled by solid electrolytes," *Advanced Functional Materials*, vol. 29, no. 27, p. 1901719, 2019.

[22] P. K. Lee, Y. Li, and D. Y. W. Yu, "Insights from studying the origins of reversible and irreversible capacities on silicon electrodes," *Journal of the Electrochemical Society*, vol. 164, p. 6206, 2017.

[23] Y. Kim, J. H. Lee, S. Cho et al., "Additive-free hollow-structured Co_3O_4 nanoparticle Li-ion battery: the origins of irreversible capacity loss," *ACS Nano*, vol. 8, no. 7, pp. 6701–6712, 2014.

[24] W. Liu, X. Zhang, Y. Huang et al., "β-MnO_2 with proton conversion mechanism in rechargeable zinc ion battery," *Journal of Energy Chemistry*, vol. 56, pp. 365–373, 2021.

[25] B. Lee, H. R. Seo, H. R. Lee et al., "Critical role of pH evolution of electrolyte in the reaction mechanism for rechargeable zinc batteries," *ChemSusChem*, vol. 9, no. 20, pp. 2948–2956, 2016.

[26] Y. Li, S. Wang, J. R. Salvador et al., "Reaction mechanisms for long-life rechargeable Zn/MnO_2 Batteries," *Chemistry of Materials*, vol. 31, no. 6, pp. 2036–2047, 2019.

[27] Y. Huang, J. Mou, W. Liu et al., "Novel insights into energy storage mechanism of aqueous rechargeable Zn/MnO_2 batteries with participation of Mn^{2+}," *Nano-Micro Letters*, vol. 11, no. 1, p. 49, 2019.

[28] M. Sathiya, A. S. Prakash, K. Ramesha, J. M. Tarascon, and A. K. Shukla, "V_2O_5-anchored carbon nanotubes for enhanced electrochemical energy storage," *Journal of the American Chemical Society*, vol. 133, no. 40, pp. 16291–16299, 2011.

[29] H. K. Song, K. T. Lee, M. G. Kim, L. F. Nazar, and J. Cho, "Recent progress in nanostructured cathode materials for lithium secondary batteries," *Advanced Functional Materials*, vol. 20, no. 22, pp. 3818–3834, 2010.

[30] A. R. C. Bredar, A. L. Chown, A. R. Burton, and B. H. Farnum, "Electrochemical impedance spectroscopy of metal oxide electrodes for energy applications," *ACS Applied Energy Materials*, vol. 3, no. 1, pp. 66–98, 2020.

[31] R. Weber, A. J. Louli, K. P. Plucknett, and J. R. Dahn, "Resistance growth in lithium-ion pouch cells with $LiNi_{0.80}Co_{0.15}Al_{0.05}O_2$ Positive electrodes and proposed mechanism for voltage dependent charge-transfer resistance," *Journal of the Electrochemical Society*, vol. 166, no. 10, pp. A1779–A1784, 2019.

[32] N. Zhang, F. Cheng, J. Liu et al., "Rechargeable aqueous zinc-manganese dioxide batteries with high energy and power densities," *Nature Communications*, vol. 8, no. 1, p. 405, 2017.

[33] J. Zhou, L. Shan, Z. Wu, X. Guo, G. Fang, and S. Liang, "Investigation of V_2O_5 as a low-cost rechargeable aqueous zinc ion battery cathode," *Chemical Communications*, vol. 54, no. 35, pp. 4457–4460, 2018.

[34] Y. Cheng, L. Luo, L. Zhong et al., "Highly reversible zinc-ion intercalation into chevrel phase Mo_6S_8 nanocubes and applications for advanced zinc-ion batteries," *ACS Applied Materials and Interfaces*, vol. 8, no. 22, pp. 13673–13677, 2016.